# Detecting and quantifying stress granules in tissues of multicellular organisms with the Obj.MPP analysis tool

Fabienne de Graeve, Eric Debreuve, Somia Rahmoun, Szilvia Ecsedi, Alia Bahri, Arnaud Hubstenberger, Xavier Descombes, Florence Besse

# Detecting and quantifying stress granules in tissues of multicellular organisms with the *Obj.MPP* analysis tool

**Running title:** Automatic detection of stress granules

Fabienne De Graeve[1], Eric Debreuve[2], Somia Rahmoun[3], Szilvia Ecsedi[1], Alia Bahri[1], Arnaud Hubstenberger[1], Xavier Descombes[3*], Florence Besse[1*]

1: Université Côte d'Azur, CNRS, Inserm, Institut de Biologie Valrose, Nice, France

2: Université Côte d'Azur, CNRS, INRIA, I3S

3: Université Côte d'Azur, INRIA, CNRS, I3S

* : correspondence to besse@unice.fr and xavier.descombes@inria.fr

## Synopsis

Stress granules (SGs) are membrane-less organelles rich in RNA and proteins that form in response to stress. Although it is known that SG characteristics depend on the nature of the stress, on cell types and on physiological states, how SG assembly and properties are controlled is still largely unclear. Here, we describe an open-source image analysis software that enables accurate detection of SGs and quantification of their properties on both epifluorescence and confocal images of intact tissues.

## Abstract

Stress Granules (SGs) are macromolecular assemblies induced by stress and composed of proteins and mRNAs stalled in translation initiation. SGs play an important role in the response to stress and in the modulation of signaling pathways. Furthermore, these structures are related to the pathological ribonucleoprotein (RNP) aggregates found in neurodegenerative disease contexts, highlighting the need to understand how they are formed and recycled in normal and pathological contexts. Although genetically tractable multicellular organisms have been key in identifying modifiers of RNP aggregate toxicity, *in vivo* analysis of SG properties and regulation has lagged behind, largely due to the difficulty of detecting SG from images of intact tissues. Here, we describe the object detector software *Obj.MPP* and show how it overcomes the limits of classical object analyzers to extract the properties of SGs from wide-field and confocal images of respectively *C. elegans* and

*Drosophila* tissues. We demonstrate that *Obj.MPP* enables the identification of genes modulating the assembly of endogenous and pathological SGs, and thus that it will be useful in the context of future genetic screens and *in vivo* studies.

**Key words:** image analysis, detection algorithm, marked point process, stress granules

## 1-Introduction

Eukaryotic cells respond to environmental stresses by inhibiting the translation of most cellular mRNAs, a process triggering the aggregation of non-translating mRNAs and associated RNA binding proteins into macromolecular cytoplasmic condensates termed stress granules (SGs) [1,2]. These dynamic macromolecular ribonucleoprotein (RNP) assemblies form very rapidly (within minutes), and are actively disassembled upon stress recovery [3]. Although SGs are highly conserved throughout evolution, their exact composition and properties, in particular their shape, appear to depend on the nature of the stress, on cell type, and on physiological parameters such as aging [4-8], indicating that their assembly is under tight molecular control. Intriguingly, a strong link has recently been established between alteration of SG biophysical properties, and the pathogenesis of end-stage neurodegenerative diseases such as amyotrophic lateral sclerosis (ALS) and frontotemporal dementia (FTD) [9-12]. A hallmark of these diseases, indeed, is the abnormal accumulation of cytoplasmic aggregates of SG-associated RNA binding proteins. For example, redistribution of TDP-43 into pathological inclusions containing SG markers is a pathological feature of most sporadic and familial forms of ALS and FTD [13,14]. Moreover, pathogenic mutations in genes encoding different SG components were shown to alter the material properties and the dynamics of granules formed by these proteins, and to induce the constitutive formation of SGs [11,15-17]. Although these studies have suggested that alterations in SG properties, biogenesis and/or recycling may contribute to disease initiation or progression, the underlying chains of molecular and cellular changes and their impact on neuron RNA homeostasis still remain largely unclear. Thus, it is crucial to uncover the regulatory properties of SGs, and to understand the relationship between normal SG assemblies and the pathological inclusions characteristic of end-stage diseases.

Genetically tractable model organisms have proven to be instrumental in elucidating the genetic and molecular bases of various cellular processes, and their physio-pathological impact in the context of living individuals. Because they are adapted to large-scale genetic or compound-based screens, invertebrate models provide in particular a powerful means to identify new genes and signaling pathways. In the context of neurodegenerative diseases, they have yielded great advances into the biological pathways impaired in disease, and the design of new therapeuthic strategies [18-20]. To date, however, most of the screens performed in invertebrates to identify regulators of ALS-related pathological processes have primarily searched for modulators of the toxicity and/or lethality induced by ectopic expression of wild-type or mutant forms of disease-causing proteins. Although lines expressing fluorescent granule markers, in particular SG markers, are available in both *Drosophila melanogaster* and *C. elegans* for imaging of various tissues [21,22], only few screens have been performed to directly identify molecules perturbing the properties of ribonucleoprotein (RNP) granules [23-25]. In these screens, phenotypic classification was done largely manually, and precise quantification of granule properties (size, number, intensity…) could not be performed. This is largely explained by the lack of adapted tools to automatically detect granular subcellular objects in images from whole mount preparations, where signal heterogeneity is typically high and signal-to-noise ratio low. Most of commonly used detection methods, indeed, are based on image thresholding, which is adapted for quantification of bright spots over the low cytoplasmic background signal characteristic of isolated cultured cells, but not for detection of granules in intact tissues [26]. Rieckher et al. described a threshold-based method to quantify P-body characteristics in *C. elegans* germline [22]. This method, however, could not extract individual granule properties from epifluorescence images, and required a manual thresholding for each confocal image analyzed. Hillebrand et al. modeled RNP granule by a mixture of gaussians on adult *Drosophila melanogaster* brains [27]. This method works efficiently in the presence of noise, but is not adapted to the detection of non-ovoid objects and is prone to induce false positives in the presence of heterogeneous background.

Here, we describe a novel open-source tool for quantitative analysis of individual SGs from intact tissues. This object detector software, that we named *Obj.MPP*, is based on the marked point process framework [28]. We show that *Obj.MPP* outcompetes other available

tools for the detection of heat-induced RNP granules on epifluorescence images from living *C. elegans* gonads. Using *Obj.MPP*, we characterized the changes in SG properties induced by inactivation of a conserved translational repressor. Highlighting the versatility of *Obj.MPP*, we also demonstrate that SG-related aggregates induced by expression of an ALS-causing mutant form of TDP-43 can be successfully detected on confocal images of *Drosophila melanogaster* larval motor neurons. Remarkably, extraction of quantitative data enabled the characterization of a gene modifying aggregate properties. Together, this study demonstrates that *Obj.MPP* is a powerful and versatile image analysis tool that is well adapted to the detection of subcellular granules in complex images taken from intact tissues. Its capacity to detect poorly contrasted objects of heterogeneous size and intensities makes it a valuable tool particularly suited to the search of regulators of SG properties in genetically tractable living organisms.

## 2- Results

### 2-1- Thresholding methods are poorly adapted to the detection of SGs from tissue samples

Detecting hundreds of nanometer-sized SGs in cells imaged from intact tissues is challenging in several ways. First, fluorescently-labelled SG markers usually do not fully partition into SGs, generating a "background" cytoplasmic signal that has a heterogeneous granular texture. Second, labeled SGs exhibit a range of sizes and intensities, as well as variable shapes. Third, SGs can form clusters of closely located assemblies in contexts of intensive stress. Fourth, imaging of intact tissues usually produces images with low signal-to-noise ratio, high noise and signal heterogeneity.

To first estimate the capacity of classically-used thresholding methods to detect SGs in intact tissues, we imaged in *C. elegans* gonads RNP granules characterized by the presence of the RNA binding protein CAR-1 [23,29,30]. CAR-1 (also known as Lsm14 in human, Trailer Hitch in fruit fly, SDC6 in yeast) is an RNP granule marker that represses the translation of specific maternal mRNAs in oocytes in association with the RNA helicase CGH-1 [31,32]. In animals subjected to heat shock at 35°C for 5 hours, it clusters into heterogeneous granular structures that, in contrast to germline P-bodies, display fuzzy and irregular boundaries (Figure 1A). Heat shock-induced CAR-1 granules were imaged on living animals using an epifluorescence microscope, generating images with low signal-to-noise ratio. As illustrated

in Figure 1C-F, analyzing original images with global (*e.g.* Otsu or Shanbhag) or local (*e.g.* Midgrey or Mean) thresholding methods parameterized automatically revealed that such methods perform poorly, failing to efficiently distinguish signal from noise. To quantitatively evaluate the performance of the two most adapted local thresholding methods (Midgrey and Mean local thresholding), F1 scores were calculated using optimized parameters on a set of five representative images. To this end, the numbers of true detections, false positives and false negatives were obtained for each image by comparing the masks of detected objects (*e.g.* Figure 1G,H) with ground truth annotations generated manually by experts (*e.g.* Figure 1B; see Materials and Methods). Mean F1 scores between 0.5 and 0.6 were obtained in this condition, confirming these methods are not adapted to the detection of heat-induced granules on original epifluorescence images (Figure 1I).

As epifluorescence images typically present significant out-of-focus signal that complicates detection, we performed deconvolution and re-calculated F1 scores. Although deconvolution significantly increased signal-to-noise ratio (Figure 1A'), and thus improved detection of CAR-1 granules (Figure 1C'-H'), the mean F1 scores obtained on pre-processed images hardly reached 0.7 (Figure 1I). Such low F1 scores are in particular explained by the low capacity of thresholding methods to resolve individual granules in high density regions (*e.g.* yellow squares in Figure 1G',H', compare to A'). As revealed by inspection of detection masks, another major shortcoming of these methods was their inability to accurately recover granule shapes, even on deconvolved images (*e.g.* blue rectangles in Figure 1G',H', compare to A').

Together, these results indicate that thresholding methods are poorly adapted to the detection of SGs from intact tissues, and in particular fail to accurately detect high-density objects found on heterogeneous backgrounds. Notably, such limitations are not encountered exclusively when analyzing images from whole tissues, but are in fact also encountered when detecting SGs in cultured cells (Figure S1), highlighting the need for alternative methods that do not consider individual pixels, but rather model object signal geometry.

### 2-2- Principles of object detection using *Obj.MPP*

To address the different challenges posed by the detection of SGs, we developed the *Obj.MPP* software, that relies on the marked point process framework [28,33]. A major property

of this framework is that it fits sets of shapes on the image plane and selects the ones matching best with the pre-defined object characteristics (See Supporting Information). Thus, image properties (*e.g.* intensity) are not considered at the pixel scale, but rather at the object scale, providing robustness with respect to background signal and noise. In this framework, objects are defined by two main criteria: their shape and their radiometry. Object shapes are defined by the parameter values of selected parametric objects (*e.g.* the radius for a disc). Notably, a range of parameter values can be used, thus defining a space of marks that takes into account the variability of object size and morphology. This geometrical constraint is combined with a radiometric constraint that we termed the quality function. This function can be direct (and represents the object mean intensity) or indirect (and represents the relative intensity of the object and its surroundings) (see Supporting Information). The optimal solution, that selects the set of objects with the highest quality function values is obtained *via* a multiple birth and cut algorithm that improves the current configuration at each iteration until convergence [34]. With this algorithm, objects are first randomly added to the current configuration, and best objects are then retained within the newly constituted set of objects.

Remarkably, constraints on the spatial repartition of objects can be embedded in the model, allowing a controllable degree of overlaps between objects and optimal detection of individual objects within a cluster. Furthermore, 3D object segmentation can be implemented (Supporting Information).

**2-3- Overview of the *Obj. MPP* user interface**

The *Obj.MPP* software we present in this manuscript provides an automated workflow to detect and analyze SGs that appear as spots lighter (or darker) than the background. The Graphical User Interface (GUI) has been designed for an intuitive use and is organized in several tabs, allowing the user to easily set the parameters before image analysis and save them for future use.

After loading an image or group of images in the first tab (not shown), the user can set the detection parameters in the second one (Figure 2A). First, a shape geometry adapted to the targeted objects is chosen among available ones (circle, square, ellipse, rectangle or superquadric). The superquadrics embed all other shapes and are used when no precise

geometrical information is known on the object. For detection of SGs, disks, ellipses or superquadrics are usually preferred. Second, the ranges of shape parameters are set according to the expert knowledge on the acquired images. The available shape geometries and their parameters are summarized in the Supporting Information. Third, the quality function and its minimal acceptable value are chosen. This quality function corresponds to the object data term and selects the objects to be considered as candidates. In contrast to the prior that imposes some constraints on the configuration of objects, the data term fosters objects that fit the data. For example, the data term associated with each object can be computed as a contrast term between the pixels inside the object and the pixels in a crown surrounding the object, or by comparing the intensity gradient along the object contour with its normal. The available quality functions are presented in the Supporting Information. Candidate objects for which the quality function is higher than the selected minimal acceptable value, specified by the user in the second tab of the GUI, are then considered as detected objects provided that they do not overlap more than 20% of their size with another object. The number of iterations can be set by the user in the third tab of the GUI. Finally, different outputs can be selected in the last tab of the GUI among the following: a .csv file containing the characteristics of the detected granules (geometrical parameters, intensity), the raw image with granule contours highlighted (Figure 2C), a mask of the segmented and labeled granules (Figure 2D) and a mask of sole granule contour (data not shown). *Obj.MPP* is publicly available and can be downloaded at the following address: https://gitlab.inria.fr/edebreuv/Obj.MPP.

**2-4- *Obj. MPP* efficiently detects heat shock induced SGs in cultured cells.**

To first estimate the performance of *Obj.MPP* on a validated biological system, we induced the formation of SGs in cultured *Drosophila* S2R+ cells by heat-shocking cells for one hour at 42°C. As previously described [35], this induced the clustering of the SG marker PABP into cytoplasmic granules of heterogeneous size and intensity (compare Figure S2C and A). SGs, imaged by spinning disc confocal microscopy, were efficiently detected by *Obj.MPP*, as revealed by the high average F1 score obtained (>0.8; Figure S1J) as well as by the inspection of detection masks. As shown in Figures S1I and S2D (yellow squares), object contours were properly estimated and closely-located granules nicely individualized. To quantitatively

characterize the formation of SGs in response to heat shock, the characteristic features of objects detected *via Obj.MPP* were then extracted, revealing a more than three-fold increase in the number of PABP-positive clusters and a significant increase in their size (Figure S2E,F). These results validate the potential of *Obj.MPP* to reliably detect high density SGs and extract quantitative data.

**2-5- Performance of *Obj. MPP* in the detection of heat-induced granules on epifluorescence images of *C.elegans* gonads**

To then evaluate the performance of *Obj.MPP* on images from whole tissues, we analyzed heat-induced CAR-1 granules in *C. elegans* gonads, and compared the performance of *Obj.MPP* to that of three other algorithms considering signal geometry: the wavelet-based Spot Detector of the open-source Icy platform [36], the SPADE algorithm, another marked point process framework using a library of pre-generated objects [37] and the local maxima-based Spots function of the commercial Imaris software (Bitplane Inc). Global performances were first evaluated on original images, by FROC curves that represent for each method the trade-off between the fraction of correct detections (recall; y axis) and false positives (x axis). With this criterion, *Obj.MPP* clearly outperformed Icy Spot Detector, and performed slightly better than SPADE and the Imaris Spot function (Figures 3A and S3A). As FROC curves are obtained by varying the detection threshold (minimal acceptable value of the quality function for *Obj.MPP*), we then estimated the capacity of the different methods to consistently detect SGs in a more realistic context, by calculating F1 scores of biological images analyzed using fixed parameters. Again, the best mean F1 score was obtained for *Obj.MPP* (Figure 3C). Remarkably, *Obj.MPP* also exhibited the lowest variability in detection efficiencies, a feature also highlighted by the lowest dispersion of the optimal threshold values used to generate the FROC curves (Table S1).

Having shown that *Obj.MPP* performs better on raw epifluorescence images, we then evaluated and compared its efficiency on deconvolved images. Strikingly, image deconvolution did not improve object detection *via Obj.MPP*, but ameliorated the performance of other methods, thus reducing the gap between *Obj.MPP* and other methods (Figures 3B,C and S3B). Importantly, however, analysis of object masks revealed that *Obj.MPP* estimated better than Icy Spot Detector and Imaris Spot function the granule

contours (*e.g.* blue rectangle in Figure 3F',G',H', compare to D') and resolved better than Icy Spot Detector clusters of individual granules (*e.g.* yellow square in Figure 3F',G', compare to D'). Furthermore, *Obj.MPP*, in contrast to SPADE, was not limited by object size (data not shown; see also Figure 5).

Together, these results demonstrate that *Obj.MPP* enables efficient and stable detection of heat-induced granules on intact tissues imaged by epifluorescence microscopy. *Obj.MPP* accurately detects granules and their contour from raw images, avoiding the need for artifact-prone image pre-processing.

**2-6- The RNA binding protein PUF-5 promotes the formation of heat-induced CAR-1 granules.**

As mentioned above, comparing the subcellular distribution of GFP:CAR-1 in control animals grown at 20°C and in animals subjected to heat shock at 35°C for 5 hours revealed that heat shock induced the clustering of GFP:CAR-1 into SG-like assemblies (Figure 4A). Although the association of CAR-1 itself with SGs has not been directly tested so far, CAR-1 aggregation is consistent with the previously described accumulation of CAR-1 translation repression cofactors (such as CGH-1), and several other P-body components in heat shock-induced SGs [32,38]. To quantitatively analyze the properties of heat-induced CAR-1 granules, we ran *Obj.MPP* on a batch of 38 raw epifluorescence images using parameters defined so as to detect a minimal number of false positives in nematodes not subjected to heat shock. With these parameters, a 8 to 9-fold increase in the number of detected granules was observed upon heat shock (Figure 4B). Furthermore, analysis of granule size revealed that CAR-1 granules exhibited a range of size (Figure 4C), although the diameter of most granules was comprised between 800 and 1,300 nm.

The translational repressor PUF-5 was previously shown to be required for the coassembly of germline P-body components into membrane-less granules in *C. elegans* germline [29]. To determine whether PUF-5 is also involved in the nucleation and/or growth of heat shock-induced SGs, we down-regulated *puf-5* in GFP:CAR-1-expressing nematodes prior to heat shock and subsequently imaged gonads by epifluorescence microscopy (Figure 4A, right). Interestingly, analyzing these images with *Obj.MPP* revealed that down-regulating *puf-5* in this context led to a moderate yet significant reduction in the number of SGs formed (Figure

4B). This was accompanied by a slight shift in the distribution of SG sizes characterized by a reduction in the proportion of the biggest SGs (>35 pixels; Figures 4C and S4A, *P*<0,001 in a Fisher's exact test). These results thus suggest that PUF-5 is not strictly required for CAR-1 granule assembly in response to heat stress, but modulates the nucleation and growth of heat-induced granules.

**2-7- Performance of *Obj. MPP* in the detection of pathological SG-like assemblies on confocal images of *Drosophila* motorneurons.**

Formation of SGs is induced in response to various cellular and environmental stresses, but also upon expression of disease mutant components, as shown in various models of neurodegenerative diseases. Point mutations in the conserved RNA binding protein TDP-43, a molecule recruited to SG upon stress, were for example shown to modify the nucleo-cytoplasmic distribution of TDP-43 and generate in neurons large SG-like assemblies that are inefficiently transported to axons [13,39,40]. To characterize the properties of SGs formed upon TDP-43 expression in a genetically tractable organism, we overexpressed either the wild type or the pathological M337V form of TDP-43 in *Drosophila melanogaster* motor neurons using the UAS-Gal4 system [41]. Distribution of these Venus-tagged proteins was analyzed in third instar larvae motor neurons by confocal microscopy. As previously described [39], wild type TDP-43 mostly accumulated in the nucleus, but could be detected at low levels in the cytoplasm, forming few small granule-like structures (Figure 5A,B; arrow). In contrast, the pathological TDP-43 M337V protein significantly accumulated in the cytoplasm, generating aggregates of varying sizes (Figure 5C).

To evaluate and compare the performance of *Obj.MPP* in detecting SG-like assemblies on confocal images, we selected a set of five representative images and cropped them manually to isolate individual motoneuron cell bodies. Annotations were performed by experimented biologists to obtain ground truth data (Figure 5D). FROC curves were obtained after varying the detection threshold of *Obj.MPP*, Imaris Spots, Icy Spot Detector and SPADE. As shown in Figures 5I and S3C, all four algorithms performed better on confocal images than on epifluorescence microscopy images, the improvement being particularly noticeable for Imaris Spots and Icy Spot Detector. On these images, *Obj.MPP* performed similarly to Imaris Spots and better than Icy Spot Detector and SPADE in terms of number of correctly detected

objects (Figure 5I and Table S1). In contrast to other algorithms, however, it was able to correctly detect individual SGs within a cluster (*e.g.* yellow rectangle in Figure 5E-H). Furthermore, *Obj.MPP* performed better than Imaris in terms of accuracy of SG shape (*e.g.* blue square in Figure 5E,G) and, contrary to SPADE, did not fractionate large SGs into smaller ones (*e.g*. blue square in Figure 5H).

Altogether, these results demonstrate the versatility of *Obj.MPP*, which enables efficient detection of SGs from different origins and from intact tissues imaged by epifluorescence or confocal microscopy.

**2-8- Overexpressing TDP-43 *futsch* mRNA target reduces the proportion of TDP-43 M337V granules of high intensity.**

TDP43 is known to associate with *futsch* mRNA in *Drosophila melanogaster* and was proposed to regulate its translation at the neuromuscular junction [42]. Furthermore, *futsch* overexpression was shown to mitigate the neurotoxicity induced upon expression of ALS-causing forms of TDP-43 in motor neurons [42]. To test whether this phenotypic rescue was linked to changes in the aggregation pattern of TDP-43, we overexpressed the pathological TDP-43 M337V protein alone (Figure 6A), or together with *futsch* (Figure 6B), in *Drosophila melanogaster* motor neurons. Granules formed in both contexts were detected and characterized with *Obj.MPP* (Figure 6A'-B'). Remarkably, *futsch* overexpression did not affect the number of TDP-43 M337V-containing granules found in motor neuron cell bodies, since respectively 74 and 79 granules were on average observed per surface area in the presence and absence of *futsch* overexpression (Figure S4B). Similarly, the distribution of TDP-43 M337V granule sizes was not significantly changed upon *futsch* overexpression (Figure S4C). Interestingly however, analyzing the fluorescence intensity of TDP-43 M337V containing-granules in both conditions revealed that the fraction of high intensity granules, was significantly reduced upon *futsch* overexpression (Figures 6C and S4D), suggesting that increasing the levels of a TDP-43 mRNA target can limit the hyperaggregation of mutant proteins.

## 3- Discussion

### 3-1- *Obj.MPP* efficiently detects both physiological and pathological SGs from intact tissues

Our quantitative assessment of *Obj.MPP* performance on biological images revealed that this open-source software is very well adapted to the detection of objects of various intensities and sizes over a heterogeneous background. *Obj.MPP* clearly outcompetes methods relying on both global and local thresholding. Furthermore, it generally performs better than the three other state of the art algorithms modeling object signal properties that we tested: the Spot Detector function of the Icy platform, SPADE, and the Spots function of Imaris (two open-source and a commercial softwares respectively). As highlighted in this manuscript, *Obj.MPP* has three particularly interesting features that distinguish it from the other tested algorithms. First, it performs very well on images with low signal-to-noise ratio, making it possible to analyze epifluorescence images of whole tissues without the need of pre-processing. Second, it generates consistently high F1 scores for a fixed threshold (minimal acceptable quality), making it a tool of choice for batch analyses. Third, it efficiently resolves individual objects within clusters and accurately detects object contours. This latter property is shared with SPADE, that relies on a more exhaustive library of forms, but is limited to relatively small objects that are included in a 5X5 pixel square.

In this study, we illustrated how *Obj.MPP* can be used to extract and quantitatively compare different characteristic features (size, number, fluorescence intensity) of RNP granules present in intact *C. elegans* gonads or *Drosophila* brains, highlighting the versatility of the algorithm and its capacity to accurately detect objects of varying sizes. Thus, *Obj.MPP* is a valuable tool that can be used in the context of suppressor screens aiming at identifying compounds and/or genes involved in the assembly or recycling of physiological or pathological SGs. Notably, *Obj.MPP* is not limited to the detection of SGs and may be applied to the study of other membrane-less or vesicular organelles with various shapes and/or density. The possibility to detect superquadrics, in particular, enables the flexible search of objects with varying geometry.

### 3-2- Role of translation repressors in SG assembly

Here, we have shown in *C. elegans* that CAR-1, similarly to other P-body components [32,38], assembles into SGs in response to heat shock. This result is interesting in the context of

recent work demonstrating that CAR-1 increases animal resistance to heat shock when constitutively expressed under its non-SUMOylatable translation repressor form [43]. Thus, this raises the possibility that the aggregation of CAR-1 and repressed mRNA targets into SGs may participate to the cellular adaptation to heat shock.

As further revealed by our quantitative analysis, depleting the translation repressor PUF-5 induces a modest yet significant reduction in the number and size of SGs formed upon heat shock. This modulatory function in promoting the assembly and growth of SGs is in stark contrast with the essential role of PUF-5 in the co-assembly of germline P-body scaffold [23,29], further distinguishing SG from P-bodies. Such a difference may be explained by the fact that under heat stress, PUF-5 and its mRNA targets may represent only a subset of the larger pool of repressed mRNPs that participate to the growth of SGs. PUF-5 may also act redundantly with its paralogs PUF-6 and PUF-7 to promote the repression of specific maternal mRNA targets [29,44]. In this case, simultaneous depletion of PUF-5/6/7 may be required to trigger a more severe reduction of SG size and number.

**3-3- Suppressing the formation of pathological SG-like aggregates**

A strong connection has been established over the last past years between the progression of neurodegenerative diseases, including ALS, and the accumulation of pathological inclusions rich in RNA binding proteins and SG markers [11,45,46]. Disease-causing mutations in the conserved RNA binding protein TDP-43, for example, were shown to alter the dynamics and material properties of the macromolecular assemblages formed by TDP-43, and to induce the ectopic formation of SG-like assemblies in cells [13,15,40]. When expressed in neurons, variants of TDP-43 harboring point mutations in the C-terminal prion-like domain (*e.g.* TDP-43-M337V) form abnormally stable granules that are inefficiently transported to the distal ends of axons [39,40]. Here, we aimed at identifying conditions in which pathological TDP-43 aggregation is alleviated and set out to test the impact of *futsch/MAP1B* overexpression in *Drosophila melanogaster* motor neurons. As previously described, *futsch* mRNA is a translational target of TDP-43 whose overexpression suppresses TDP-43-induced toxicity [42]. Although biochemical fractionation experiments have indicated that overexpression of *futsch* significantly reduced the amount of both wild-type and mutant TDP-43 in urea-insoluble fractions [42], whether this reflected a decreased propensity of TDP-43 to assemble into SG-like

aggregates remained unclear. Our quantitative analysis of fluorescent TDP-43 M337V granule properties revealed that *futsch* overexpression does not significantly impact on the number of SG-like granules, but induces a significant decrease in the proportion of TDP-43 M337V-containing granules of high fluorescence intensity (Figure 6C). This indicates that increasing the level of a target mRNA of TDP-43 somehow inhibits the hyper-recruitment of TDP-43 M337V into pathological assemblies, consistent with the previously observed increase in solubility [42]. How the overexpression of *futsch* alleviates the aggregation of TDP-43-M337V mutants remains to be investigated, but a possibility is that it may buffer the demixing reaction underlying granule assembly by increasing RNA/protein ratios [47].

## 4- Materials and methods

### 4-1- Estimation of algorithm performances

Single oocytes of *C. elegans* gonads, single motoneuron cell bodies of *Drosophila melanogaster* and single cultured *Drosophila* S2R+ cells were cropped from original images, manually annotated by two authors of the manuscript and validated (or corrected) by an expert external to this study. Only original images were annotated. The same annotations were used when evaluating the method performances on original or deconvolved images. Were considered as granules, rounded to ovoid objects with defined edges and intensity above a threshold fixed for each image type (*C. elegans* : 2600 ; *Drosophila melanogaster*: 400 ; S2R+ cell line: 5500). Clustered objects were discriminated with the Fiji Plot Profile tool (https://imagej.net, [48]). The central pixel (barycenter) of each granule was marked using the Fiji multi-point tool (https://imagej.net, [48]). To calculate F1 scores, granule spatial coordinates were recovered in a .csv file and compared to the binary masks generated by the different algorithms. Granules were considered as correctly detected (True Positive) when their barycenter overlapped with a single detection in the mask, and as missed (False Negative) when they did not. In case several barycenters simultaneously overlapped with a single detection, one of the barycenters was considered as correct, the others as being under-detected (False Negative). Detections that did not overlap with a barycenter were considered as being invented (False Positive). True/false positives and negatives were defined at the granule level, independently of size or geometry, thus evaluating the detector ability to spot a granule. Detector's efficiencies were evaluated by FROC curves, which display recall

values in function of the number of false positives detected. Recall = True Positives/(True Positives + False Negative). These curves were obtained as previously described [49,50], by varying the threshold (minimal acceptable value of the quality function) and determining for each threshold value the number of True positives and False negatives. Because of the variability of biological image properties, we generated one FROC curve per annotated image (*i.e* five per algorithm). For the sake of clarity, we plotted for each algorithm tested the average of the five individual FROC curves. This averaging must be understood as the averaging of recalls at a given false positive number. F1 scores were calculated as follow: F1 = 2(precision x recall)/(precision + recall), where precision = True Positives/(True Positives + False Positives).

*Obj.MPP* and SPADE generate masks containing labeled objects. Since Imaris Spots does not provide a binary mask, masks were created using available information on spot coordinates and radius. Objects in the binary masks generated by global and local thresholds, Icy spot Detector and Imaris were labeled using the Fiji plugin Morphology [51]. In contrast to SPADE and Icy Spot Detector, objects encompassing the image borders are not detected by *Obj.MPP*, whereas Imaris offers both options. SPADE and Icy Spot Detector results were thus curated to eliminate false positives using MorphoLibJ [52].

**4-2- *C. elegans* lines, preparation and imaging**

C. *elegans* strains were maintained at 20°C by standard methods [53]. The P*pie-1*::GFP::CAR-1::UTR*pie-1* transgenic strain expresses a fusion of GFP to the N-terminus of full length CAR-1 in the germ line, under the control of the *pie-1* promoter and 3'UTR. The transgenic animals were generated by microparticle bombardment of the Bristol N2 strain (gift of J. Squirrell) [29,30]. To perform gene silencing, RNAi were delivered into the animals by feeding as previously described [54]. We used a L4440 cloning vector (pTE7.30) derived from *C. elegans* RNAi genome library [55] (source Bioscience) with either *puf-5(RNAi),* (L4440 vector inserted with full length *puf-5* cDNA), or a *non-targeting(RNAi)*, (L4440 empty vector), as a control experiment [54]. L4 larvae were transferred onto RNAi feeding plates and grown for 48h at 20°C. Worms treated with *puf-5(RNAi)* and *non-targeting(RNAi)* were processed in parallel. To induce heat shock SGs, animals were further incubated at 35°C for 5 hours. For live imaging, nematodes were anesthetized in PBS with 30mM $NaN_3$ and mounted onto 2%

agarose pads with coverslip [54]. All the images were acquired at room temperature using an Olympus Bx61 epifluorescence microscope equipped with a filter specific for GFP (green fluorescence) and a 40x Uplan FLNO objective.

### 4-3- *Drosophila* lines, preparation and imaging

The *UAS-Venus-TDP-43 wild-type* and *UAS-Venus-TDP-43-M337V* fly lines were provided by Paul Taylor (St. Jude Children's Research Hospital Tennessee) [39]. The *P{EP}futschEP1419w1118* fly line was provided by Daniela C. Zarnescu (University of Arizona, Tucson, Arizona) [42]. The *P{EP}futsch$^{EP1419}w^{1118}$* and *UAS-Venus-TDP-43-M337V* transgenes were combined to generate the *P{EP}futsch$^{EP1419}w^{1118}$ ; ; UAS-Venus-TDP-43-M337V* fly line. The OK371-Gal4 fly line was provided by Serge Birman (ESPCI, Paris) and used to drive expression in motor neurons and glutamatergic centers in the brain [56]. Flies were raised under standard conditions at 22°C.

Wandering 3$^{rd}$ instar *Drosophila melanogaster* larvae were dissected in PBS 1X, fixed for 20 minutes in PBS 1X, Formaldehyde 4% (at RT), and washed three times for 30 minutes in PBS1X (at RT). The brain lobes and ventral nerve cord were mounted in Vectashield ® Antifade Mounting Medium (Vector Laboratories, USA) on diagnostic microscope slides ER-308B-CE24 (Thermo Scientific), and imaged using the 488 laser line, the sensitive internal detector (GaAsp) and the Plan-Apochromat 63X/1.40 oil DIC objective of a Zeiss LSM880 confocal microscope.

### 4-4- *Drosophila* S2R+ cells

*Drosophila* S2R+ cells were plated in LabTek chambered slides at a density of $5.10^6$ cells/well and incubated for one day before heat shock (1 hour, 42°C). Cells were then fixed in 4% paraformaldehyde for 10 minutes, washed and permeabilized in PBS/0.1% Triton (PBT), blocked in PBT supplemented with 1% BSA and incubated overnight with rabbit anti-PABP antibodies (1:500; generous gift from C. Lim) in PBT supplemented with 0.1% BSA. Cells were then washed with PBT, incubated with Cy3-conjugated anti-rabbit antibody (1:500) in PBT/0.1% BSA for 1–2 h, and washed once before DAPI labeling (5 minutes, 5µg/mL). After two washes in PBT, cells were mounted in Vectashield for imaging. Images were acquired on a Spinning Disc confocal microscope equipped with a Yokogawa CSU-X1

confocal head, and a iXON DU-897-BV EMCCD camera (Andor technology), using a UPLSAPO 100X oil 1.4 NA objective.

**4-5- Image deconvolution**

Images were deconvolved with Huygens professional 19.04 software and the following settings:

*C. elegans* images: sampling intervals : x, y : 161,25 nm; NA: 1,3; Lens immersion: oil 1,518; Embedding medium: water 1,338; Objective quality: good; Microscope type: widefield; Emission wavelength: 525; Multi photon excitation: 1; Background estimation manually : 2160; Maximum iterations: 50; Signal-to-noise ratio : 30; Quality threshold 0,01; Iteration mode optimized; Bleaching correction off; Brick layout Auto.

*Drosophila melanogaster* images: sampling intervals : x, y : 73,216 nm; NA: 1,4; Lens immersion: oil 1,518; Embedding medium: vectashield: 1,45; Objective quality: good; Microscope type: confocal; Backprojected pinhole 260; Excitation wavelength : 488; Emission wavelength: 520; Multi photon excitation: 1; Excitation fill factor : 2; Background estimation manually: 100; Maximum iterations: 50; Signal-to-noise ratio: 15; Quality threshold 0,01; Iteration mode optimized; Bleaching correction off; Brick layout Auto.

S2R+ images: sampling intervals : x, y : 135,4 nm; NA: 1,4; Lens immersion: oil 1,515; Embedding medium: vectashield: 1,45; Objective quality: good; Microscope type: confocal; Backprojected pinhole 280; Excitation wavelength : 561; Emission wavelength: 610; Multi photon excitation: 1; Excitation fill factor : 2; Background estimation manually : 1500; Maximum iterations: 50; Signal-to-noise ratio : 20; Quality threshold 0,01; Iteration mode optimized; Bleaching correction off; Brick layout Auto.

**Acknowledgments**

This work was supported by the ANR (through the RNAGRIMP grant) and the JPND program (through the FlySMALS grant). We thank L. Palin for excellent technical assistance, Kavya Vinayan Pushpalatha for her help in granule annotation, C. Perrois for the images of SGs in S2R+ cells, and the PRISM Imaging Facility for use of their microscopes and support. We are grateful to the Bloomington Drosophila Stock Center, P. Taylor and D. Zarnerscu for reagents.

**Conflict of interest**

The authors declare no conflict of interest.

## References


1. Anderson P, Kedersha N. Stress granules: the Tao of RNA triage. *Trends Biochem Sci.* 2008;33(3):141-150.
2. Buchan JR, Parker R. Eukaryotic stress granules: the ins and outs of translation. *Mol Cell.* 2009;36(6):932-941.
3. Protter DSW, Parker R. Principles and Properties of Stress Granules. *Trends Cell Biol.* 2016;26(9):668-679.
4. Buchan JR, Yoon JH, Parker R. Stress-specific composition, assembly and kinetics of stress granules in Saccharomyces cerevisiae. *J Cell Sci.* 2011;124(Pt 2):228-239.
5. Jud MC, Czerwinski MJ, Wood MP, et al. Large P body-like RNPs form in C. elegans oocytes in response to arrested ovulation, heat shock, osmotic stress, and anoxia and are regulated by the major sperm protein pathway. *Dev Biol.* 2008;318(1):38-51.
6. Mahboubi H, Kodiha M, Stochaj U. Automated detection and quantification of granular cell compartments. *Microsc Microanal.* 2013;19(3):617-628.
7. Markmiller S, Soltanieh S, Server KL, et al. Context-Dependent and Disease-Specific Diversity in Protein Interactions within Stress Granules. *Cell.* 2018;172(3):590-604 e513.
8. Moujaber O, Mahboubi H, Kodiha M, et al. Dissecting the molecular mechanisms that impair stress granule formation in aging cells. *Biochim Biophys Acta Mol Cell Res.* 2017;1864(3):475-486.
9. Fan AC, Leung AK. RNA Granules and Diseases: A Case Study of Stress Granules in ALS and FTLD. *Adv Exp Med Biol.* 2016;907:263-296.
10. Lagier-Tourenne C, Polymenidou M, Cleveland DW. TDP-43 and FUS/TLS: emerging roles in RNA processing and neurodegeneration. *Hum Mol Genet.* 2010;19(R1):R46-64.
11. Li YR, King OD, Shorter J, Gitler AD. Stress granules as crucibles of ALS pathogenesis. *J Cell Biol.* 2013;201(3):361-372.
12. Ramaswami M, Taylor JP, Parker R. Altered ribostasis: RNA-protein granules in degenerative disorders. *Cell.* 2013;154(4):727-736.
13. Liu-Yesucevitz L, Bilgutay A, Zhang YJ, et al. Tar DNA binding protein-43 (TDP-43) associates with stress granules: analysis of cultured cells and pathological brain tissue. *PLoS One.* 2010;5(10):e13250.
14. Wolozin B. Regulated protein aggregation: stress granules and neurodegeneration. *Mol Neurodegener.* 2012;7:56.
15. Johnson BS, Snead D, Lee JJ, McCaffery JM, Shorter J, Gitler AD. TDP-43 is intrinsically aggregation-prone, and amyotrophic lateral sclerosis-linked mutations accelerate aggregation and increase toxicity. *J Biol Chem.* 2009;284(30):20329-20339.
16. Murakami T, Qamar S, Lin JQ, et al. ALS/FTD Mutation-Induced Phase Transition of FUS Liquid Droplets and Reversible Hydrogels into Irreversible Hydrogels Impairs RNP Granule Function. *Neuron.* 2015;88(4):678-690.

17. Patel A, Lee HO, Jawerth L, et al. A Liquid-to-Solid Phase Transition of the ALS Protein FUS Accelerated by Disease Mutation. *Cell.* 2015;162(5):1066-1077.
18. Bonini NM, Gitler AD. Model organisms reveal insight into human neurodegenerative disease: ataxin-2 intermediate-length polyglutamine expansions are a risk factor for ALS. *J Mol Neurosci.* 2011;45(3):676-683.
19. McGurk L, Berson A, Bonini NM. Drosophila as an In Vivo Model for Human Neurodegenerative Disease. *Genetics.* 2015;201(2):377-402.
20. Sin O, Michels H, Nollen EA. Genetic screens in Caenorhabditis elegans models for neurodegenerative diseases. *Biochim Biophys Acta.* 2014;1842(10):1951-1959.
21. Lowe N, Rees JS, Roote J, et al. Analysis of the expression patterns, subcellular localisations and interaction partners of Drosophila proteins using a pigP protein trap library. *Development.* 2014;141(20):3994-4005.
22. Rieckher M, Tavernarakis N. P-body and Stress Granule Quantification in Caenorhabditis elegans. *Bio Protoc.* 2017;7(2).
23. Hubstenberger A, Cameron C, Noble SL, Keenan S, Evans TC. Modifiers of solid RNP granules control normal RNP dynamics and mRNA activity in early development. *J Cell Biol.* 2015;211(3):703-716.
24. Voronina E, Seydoux G. The C. elegans homolog of nucleoporin Nup98 is required for the integrity and function of germline P granules. *Development.* 2010;137(9):1441-1450.
25. Wood MP, Hollis A, Severance AL, Karrick ML, Schisa JA. RNAi Screen Identifies Novel Regulators of RNP Granules in the Caenorhabditis elegans Germ Line. *G3 (Bethesda).* 2016;6(8):2643-2654.
26. Smal I, Loog M, Niessen W, Meijering E. Quantitative comparison of spot detection methods in fluorescence microscopy. *IEEE Trans Med Imaging.* 2010;29(2):282-301.
27. Hillebrand J, Pan K, Kokaram A, Barbee S, Parker R, Ramaswami M. The Me31B DEAD-Box Helicase Localizes to Postsynaptic Foci and Regulates Expression of a CaMKII Reporter mRNA in Dendrites of Drosophila Olfactory Projection Neurons. *Front Neural Circuits.* 2010;4:121.
28. Descombes X. Stochastic geometry for image analysis. *Wiley-VCH.* 2011.
29. Hubstenberger A, Noble SL, Cameron C, Evans TC. Translation repressors, an RNA helicase, and developmental cues control RNP phase transitions during early development. *Dev Cell.* 2013;27(2):161-173.
30. Squirrell JM, Eggers ZT, Luedke N, et al. CAR-1, a protein that localizes with the mRNA decapping component DCAP-1, is required for cytokinesis and ER organization in Caenorhabditis elegans embryos. *Mol Biol Cell.* 2006;17(1):336-344.
31. Audhya A, Hyndman F, McLeod IX, et al. A complex containing the Sm protein CAR-1 and the RNA helicase CGH-1 is required for embryonic cytokinesis in Caenorhabditis elegans. *J Cell Biol.* 2005;171(2):267-279.
32. Noble SL, Allen BL, Goh LK, Nordick K, Evans TC. Maternal mRNAs are regulated by diverse P body-related mRNP granules during early Caenorhabditis elegans development. *J Cell Biol.* 2008;182(3):559-572.
33. Descombes X. Multiple objects detection in biological images using a marked point process framework. *Methods.* 2017;115:2-8.
34. Gamal Eldin A, Descombes X, Charpiat G. A fast Multiple Birth and Cut algorithm using belief propagation *Proceedings of the 18th IEEE International Conference on Image Processing, ICIP 2011.* 2011.

35. Farny NG, Kedersha NL, Silver PA. Metazoan stress granule assembly is mediated by P-eIF2alpha-dependent and -independent mechanisms. *RNA.* 2009;15(10):1814-1821.
36. Olivo-Marin JC. Extraction of spots in biological images using multiscale products. *Pattern Recognition.* 2002;35:1989-1996.
37. Cedilnik N, Debreuve E, De Graeve F, Besse F, Descombes X. SPADE: A Small Particle Detection Method Using A Dictionary Of Shapes Within The Marked Point Process Framework *IEEE International Symposium on Biomedical Imaging (ISBI).* 2018.
38. Jud M, Razelun J, Bickel J, Czerwinski M, Schisa JA. Conservation of large foci formation in arrested oocytes of Caenorhabditis nematodes. *Dev Genes Evol.* 2007;217(3):221-226.
39. Alami NH, Smith RB, Carrasco MA, et al. Axonal transport of TDP-43 mRNA granules is impaired by ALS-causing mutations. *Neuron.* 2014;81(3):536-543.
40. Gopal PP, Nirschl JJ, Klinman E, Holzbaur EL. Amyotrophic lateral sclerosis-linked mutations increase the viscosity of liquid-like TDP-43 RNP granules in neurons. *Proc Natl Acad Sci U S A.* 2017;114(12):E2466-E2475.
41. Brand AH, Perrimon N. Targeted gene expression as a means of altering cell fates and generating dominant phenotypes. *Development.* 1993;118(2):401-415.
42. Coyne AN, Siddegowda BB, Estes PS, et al. Futsch/MAP1B mRNA is a translational target of TDP-43 and is neuroprotective in a Drosophila model of amyotrophic lateral sclerosis. *J Neurosci.* 2014;34(48):15962-15974.
43. Moll L, Roitenberg N, Bejerano-Sagie M, et al. The insulin/IGF signaling cascade modulates SUMOylation to regulate aging and proteostasis in Caenorhabditis elegans. *Elife.* 2018;7.
44. Lublin AL, Evans TC. The RNA-binding proteins PUF-5, PUF-6, and PUF-7 reveal multiple systems for maternal mRNA regulation during C. elegans oogenesis. *Dev Biol.* 2007;303(2):635-649.
45. Formicola N, Vijayakumar J, Besse F. Neuronal RNP granules: dynamic sensors of localized signals. *Traffic.* 2019;in press.
46. Taylor JP, Brown RH, Jr., Cleveland DW. Decoding ALS: from genes to mechanism. *Nature.* 2016;539(7628):197-206.
47. Maharana S, Wang J, Papadopoulos DK, et al. RNA buffers the phase separation behavior of prion-like RNA binding proteins. *Science.* 2018;360(6391):918-921.
48. Schindelin J, Arganda-Carreras I, Frise E, et al. Fiji: an open-source platform for biological-image analysis. *Nat Methods.* 2012;9(7):676-682.
49. Bunch PC, F. HJ, Sanderson GK, Simmons AH. A free-response approach to the measurement and characterization of radiographic-observer performance. *Journal of Applied Photographic Engineering.* 1978;4(4):165-171.
50. Egan JP, Greenberg GZ, Schulman AI. Operating characteristics, signal delectability, and the methods of free response. *Journal of the Acoustical Society of America* 1961;33(8):993-1007.
51. Landini G. Advanced shape analysis with ImageJ. *Proceedings of the Second ImageJ User and Developer Conference.* 2008:116-121.
52. Legland D, Arganda-Carreras I, Andrey P. MorphoLibJ: integrated library and plugins for mathematical morphology with ImageJ. *Bioinformatics* 2016;32(22):3532-3534.
53. Brenner S. The genetics of Caenorhabditis elegans. *Genetics.* 1974;77(1):71-94.

54. Hubstenberger A, Cameron C, Shtofman R, Gutman S, Evans TC. A network of PUF proteins and Ras signaling promote mRNA repression and oogenesis in C. elegans. *Dev Biol.* 2012;366(2):218-231.
55. Kamath RS, Fraser AG, Dong Y, et al. Systematic functional analysis of the Caenorhabditis elegans genome using RNAi. *Nature.* 2003;421(6920):231-237.
56. Mahr A, Aberle H. The expression pattern of the Drosophila vesicular glutamate transporter: a marker protein for motoneurons and glutamatergic centers in the brain. *Gene Expr Patterns.* 2006;6(3):299-309.

**Figure legends**

**Figure 1. Performance of global and local thresholding methods in the detection of heat-induced granules on original and deconvolved epifluorescence images of *C. elegans* gonads**

(A,A') GFP:CAR1 distribution in an individual oocyte of an adult *C. elegans* subjected to heat shock. Gonads were imaged using an epifluorescence microscope and individual oocytes manually cropped and annotated by experimented biologists (B,B'). Original images are on top, deconvolved images are on the bottom. Scale bar: 3 μm. (C-H') Masks of the objects detected with Otsu (C,C') or Shanbhag (D,D') automatic global thresholding, Midgrey (E,E') or Mean (F,F') automatic local thresholding and Midgrey (G,G') or Mean (H,H') optimized local thresholding. Parameters used in Fiji for G:radius = 14, parameter 1 = -6 ; G':radius = 15, parameter 1 = -9 and H:radius = 13, parameter 1 = -7 ; H':radius = 6, parameter 1 = -27. The yellow square highlights clustered granules that are not individualized (G', H', compare to A'). The blue rectangle highlights granules whose contours are not properly defined (G', H', compare to A'). (I) Distribution of F1 scores obtained on a set of five representative original (black) or deconvolved (grey) images, using the same parameters as in G-H'. Box plots are represented using the "min to max" convention, where the middle line defines the median and the whiskers go down to the smallest value and up to the largest. Individual data points are represented as symbols.

**Figure 2. *Obj. MPP* user interface**

(A) Parameters describing object shape (geometry under "object" and dimensions under "ranges") and data term (or quality) are defined in the second tab. (B) Example of a raw image. (C,D) Output files include (among others) the raw image with detected object contours (C) and a mask of the detected and labeled objects. For the sake of clarity, labeled objects were colored with Fiji plugin MorphoLibj (D).

**Figure 3. Performance of *Obj.MPP* in the detection of stress granules on original and deconvolved epifluorescence images of *C. elegans* gonads**

(A,B) Best sigmoidal fits on the average FROC curves obtained with the different tested algorithms run on five representative original (A) or deconvolved (B) images. For the sake of clarity, the raw data (shown in Figure S3A,B) were extrapolated to sigmoïds using a 1/(1+exp(-x)) function. Parameters used for the analysis were the following: *Obj.MPP* (1500 iterations, 50 births per iteration, Object type: superquadric, Object ranges: semi_minor_axis_range (2, 4, 0.25), major_minor_ratio_range (1.0, 1.5, 0.025), exponent_range (1.5, 2.5, 0.1), angle_degree_range (0.0, 179.9, 5.0), Object quality: bright on dark gradient, min_quality range : variable ); Imaris spots (different spots sizes, estimated diameter 2 μm, background substraction, Filters : "Quality" above threshold fixed manually and variable, Filter for objects close to image border (0,5 μm), Spot region from local contrast, diameter from region volume, radius scale =1); Icy Spot Detector (Detect bright spots over dark background, Force use of 2D wavelets, scale 2, object size ~ 3 pixels (original images), scale 1, object size 1 ~ pixels (deconvolved images), Wavelet Adaptive Treshold sensitivity variable, Size filtering minimum 4 pixels); SPADE (median filter and threshold range variable). (C) Distribution of F1 scores obtained on original (black) or deconvolved (grey) images using the same parameters as in (A,B) and the following thresholds: original images: *Obj.MPP*: 0.85, Icy Spot Detector : 180, Imaris : 95, SPADE : 0.025; deconvolved images: *Obj.MPP*: 1.1, Icy Spot Detector : 200, Imaris : 2400, SPADE : 0.15. Box plots are represented using the "min to max" convention, where the middle line defines the median and the whiskers go down to the smallest value and up to the largest. Individual data points are represented as symbols. (D,D') GFP:CAR1 distribution in an individual oocyte of an adult *C. elegans* subjected to heat shock. Gonads were imaged using an epifluorescence microscope and individual oocytes manually cropped and annotated by experimented biologists (E,E'). Scale bar: 3 μm. (F-I') Masks of the objects detected with *Obj.MPP* (F,F'), Icy Spot Detector (G,G'), Imaris Spots (H,H') and SPADE (I,I'). The yellow square highlights granules that are not individualized by the Icy Spot Detector (G,G'). The blue rectangle highlights granules whose contours are not properly defined by the Imaris Spots function (H,H').

**Figure 4. Heat-induced granules form less efficiently in *C. elegans* gonad after downregulation of PUF-5.**

(A) GFP:CAR1 distribution in individual oocytes of adult *C. elegans* subjected (middle and right) or not (left) to heat shock (HS). The image on the right was taken from a nematode subjected to *puf-5* RNAi. The white arrow in A points to a perinuclear P granule. Scale bar: 3 μm. (B) Distribution of granule numbers normalized by oocyte area. Images of all three conditions were analyzed with *Obj.MPP* parameterized so as to detect a minimal number of false positives (mostly perinuclear P granules) in the control images (Quality function = 1.45). For this analysis, we made use of a mask to restrict the area of SG detection to oocytes. Box plots are represented using the "min to max" convention, where the middle line defines the median and the whiskers go down to the smallest value and up to the largest. *, $P<0.05$; ***, $P<0.001$ (One-way ANOVA test followed by a Sidak's multiple comparison test). Numbers of gonads analyzed per condition: 60 (-HS), 38 (+HS) and 39 (+HS; *puf-5* RNAi). a.u. stands for arbitrary unit. (C) Frequency distribution of the size (in pixels) of heat-induced granules, in the absence (red) or presence (black) of *puf-5* RNAi. Numbers of granules analyzed: 680 and 533 for the +HS and +HS; *puf-5* RNAi conditions respectively. Parameters used for detection with *Obj.MPP* are described in the legend of Figure 3.

**Figure 5. Performance of *Obj.MPP* in the detection of pathological stress granules on confocal images of *Drosophila* motor neurons**

(A) Distribution of Venus-tagged wild-type TDP-43 in the cell body of a motor neuron from a third instar *Drosophila melanogaster* larva. A single section confocal image is shown. (B) Mask of the granules detected by *Obj.MPP* on the image shown in A. The white arrows in (A) and (B) point to a cytoplasmic granule, the plain and dotted lines delimit the contour of the cell and nucleus respectively. (C) Distribution of Venus-tagged ALS-causing M337V TDP-43 mutant in the cell body of a motor neuron from a third instar *Drosophila melanogaster* larva. Scale bar in A,C: 3 μm. (D) Image shown in (C) annotated by experimented biologists. (E-H) Masks of the objects detected with *Obj.MPP* (E), Icy Spot Detector (F), Imaris Spots (G) and SPADE (H). The yellow rectangle highlights a region illustrating that *Obj.MPP* performs better than the other algorithms. The blue square highlights granules whose contours were not properly captured by Imaris Spots (G) and which got fragmented by SPADE (H). (I) Best sigmoidal fits on average FROC curves obtained with the different tested algorithms run on five representative images. For the sake of clarity, the raw data (shown in Figure S3C) were

extrapolated to sigmoïds using a 1/(1+exp(-x)) function. Parameters used for the analysis were the following: *Obj.MPP* (1500 iterations, 50 births per iteration, Object type: super quadric, Object ranges: semi_minor_axis_range (2, 4, 0.25), major_minor_ratio_range (1.0, 1.5, 0.025), exponent_range (1.5, 2.5, 0.1), angle_degree_range (0.0, 179.9, 5.0), Object quality: bright on dark gradient, min_quality range : variable); Imaris spots (different spots sizes, estimated diameter 0.164 μm, background substraction, Filters : "Quality" above threshold fixed manually and variable, Filter for objects close to image border (0,036 μm), Spot region from local contrast, diameter from region volume, radius scale =1); Icy Spot Detector (Detect bright spots over dark background, Force use of 2D wavelets, scale 2, object size 3 pixels, Wavelet Adaptive Treshold sensitivity variable, Size filtering minimum 4 pixels); SPADE (median filter and threshold range variable).

**Figure 6. The proportion of bright TDP-43 M337V granule-like assemblies decreases upon *futsch* overexpression.**

(A-B) Distribution of ALS-causing M337V mutant TDP-43 in motor neuron cell bodies of third instar *Drosophila melanogaster* larvae. *futsch* was overexpressed in (B). Single section confocal images are shown. The plain and dotted lines delimit the contour of the cell and nucleus respectively. Scale bar: 3 μm. Images of both genotypes were analyzed with *Obj.MPP* (1500 iterations, 50 births per iteration, Object type : superquadric, Object ranges : semi_minor_axis_range (2, 4, 0.25), major_minor_ratio_range (1.0, 1.5, 0.025), exponent_range (1.5, 2.5, 0.1), angle_degree_range (0.0, 179.9, 5.0), Object quality : bright on dark gradient, min_quality: 1,5). Masks were used to restrict the area of SG-like assembly detection to cell bodies under study. (C) Frequency distribution of TDP-43 M337V granules according their maximal intensity (in arbitrary units) in the absence (red) or presence (black) of *futsch* overexpression. Numbers of granules analyzed: 851 for TDP-43 M337V sole expression and 1068 for TDP-43 M377V and *futsch* overexpression.

**Listing of Supplemental Materials**

**- Supporting Information:** Available object shapes, principles of the Marked-Point Process, 3D segmentation *via* the Marked Point Process

**- Supplemental Figure legends**

**- Figure S1. *Obj.MPP* outperforms global and local thresholding methods in the detection of heat shock induced PABP-containing granules in *Drosophila* S2R+ cell line.**

**- Figure S2. *Obj.MPP* detects an increase in both number and size of PABP-containing granules in *Drosophila* S2R+ cells upon heat shock.**

**- Figure S3. FROC curves (raw data)**

**- Figure S4. Characteristics of heat-induced SGs in *C. elegans* and of TDP-43 M337V granule-like assemblies in *Drosophila menalogaster*.**

**- Table S1. Best F1 scores obtained by the algorithms for the different biological images tested**

**- Supplemental Materials:** source folder

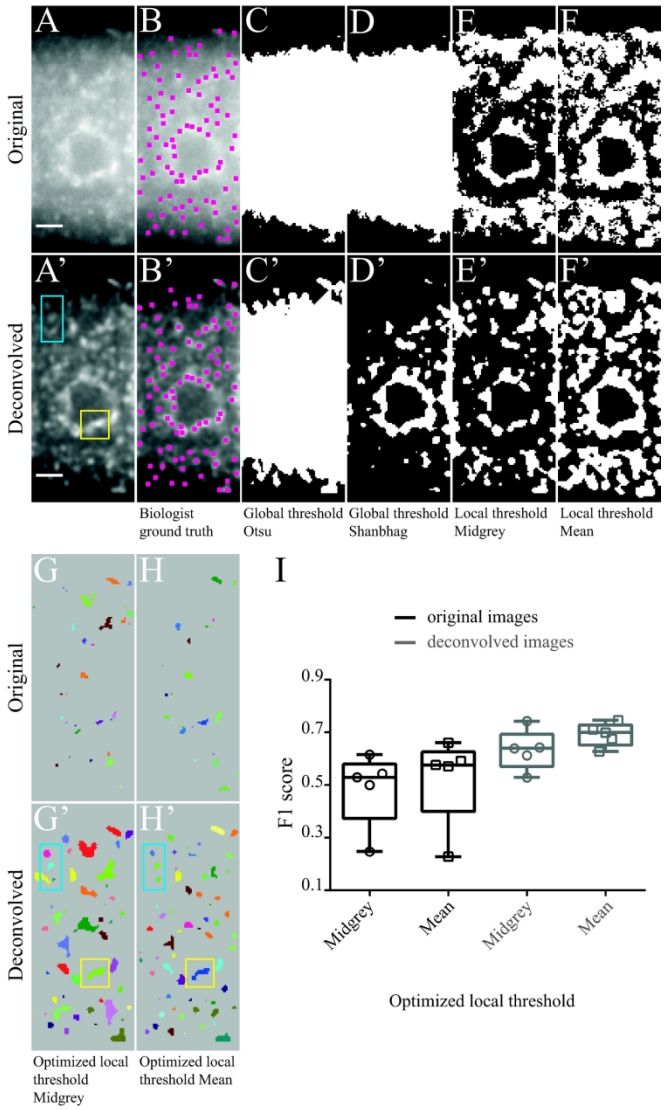


Figure 1

Figure 1. Performance of global and local thresholding methods in the detection of heat-induced granules on original and deconvolved epifluorescence images of C. elegans gonads

155x283mm (300 x 300 DPI)

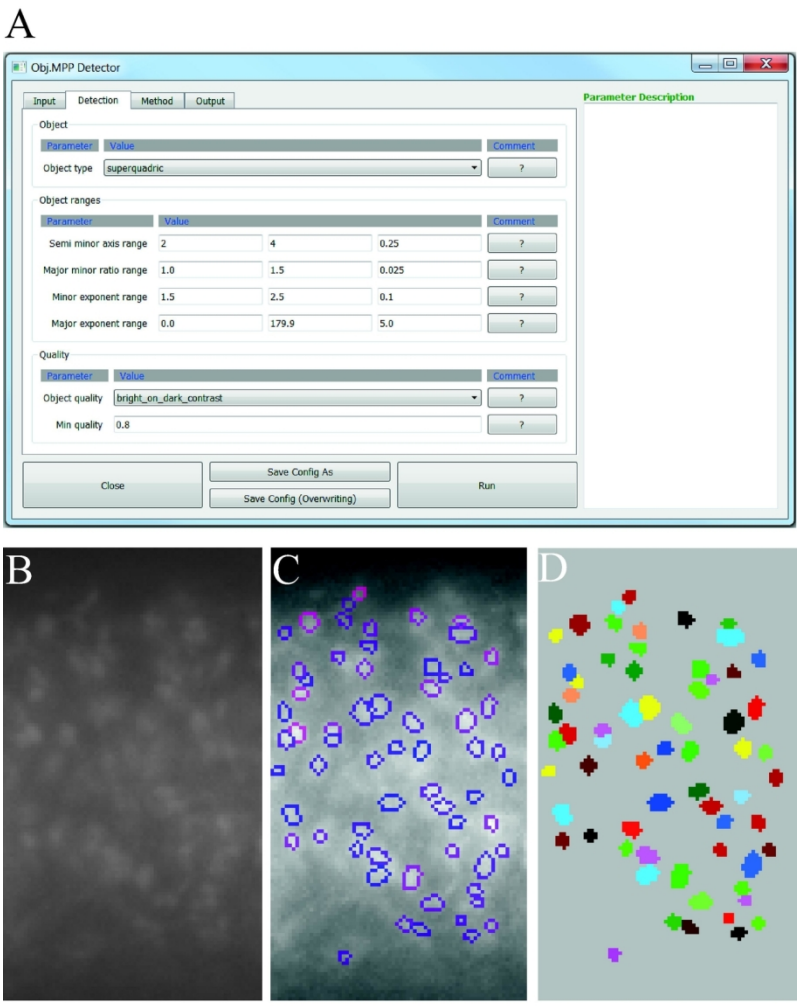


Figure 2

Figure 2. Obj. MPP user interface

117x178mm (300 x 300 DPI)

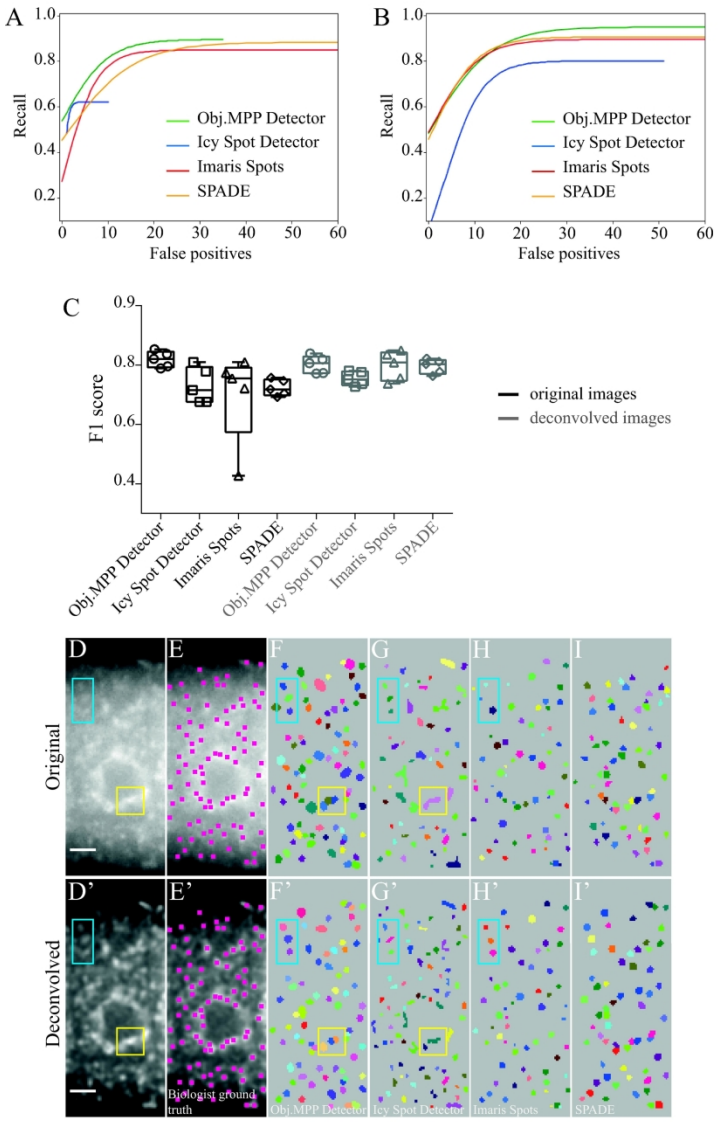


Figure 3

Figure 3. Performance of Obj.MPP in the detection of stress granules on original and decon-volved epifluorescence images of C. elegans gonads

180x293mm (300 x 300 DPI)

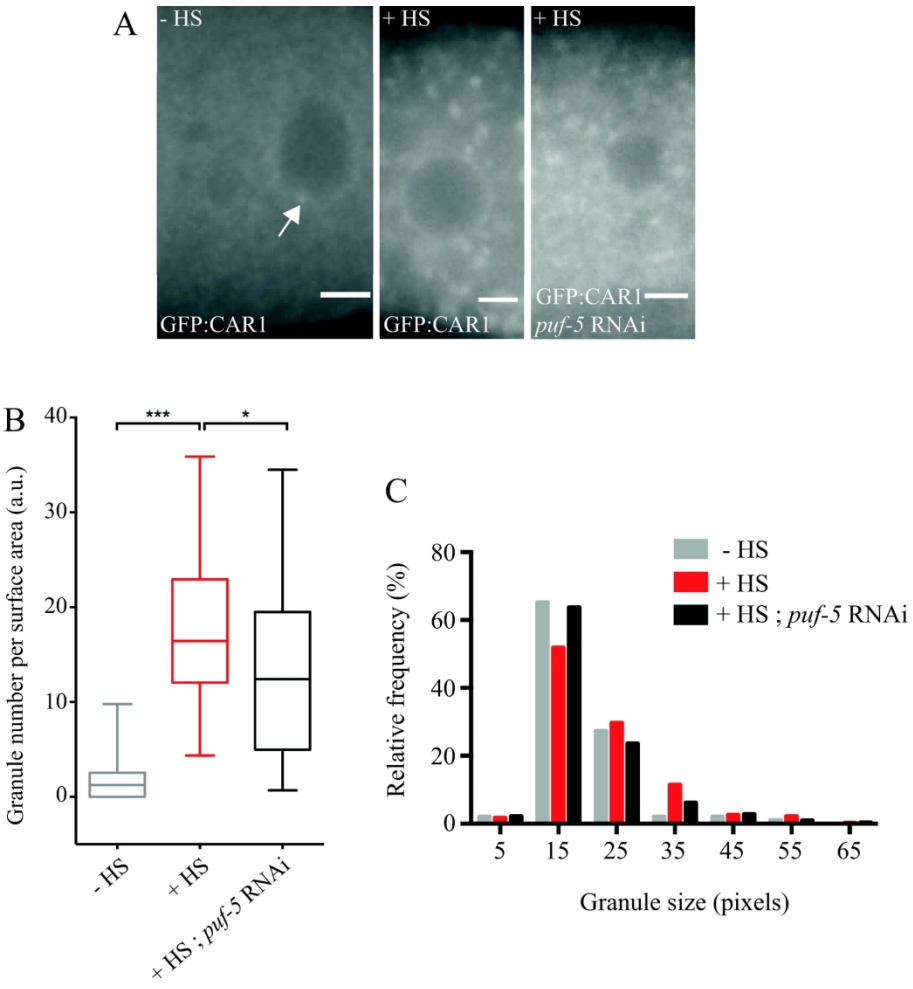


Figure 4

Figure 4. Heat-induced granules form less efficiently in C. elegans gonad after downregulation of PUF-5.

165x218mm (300 x 300 DPI)

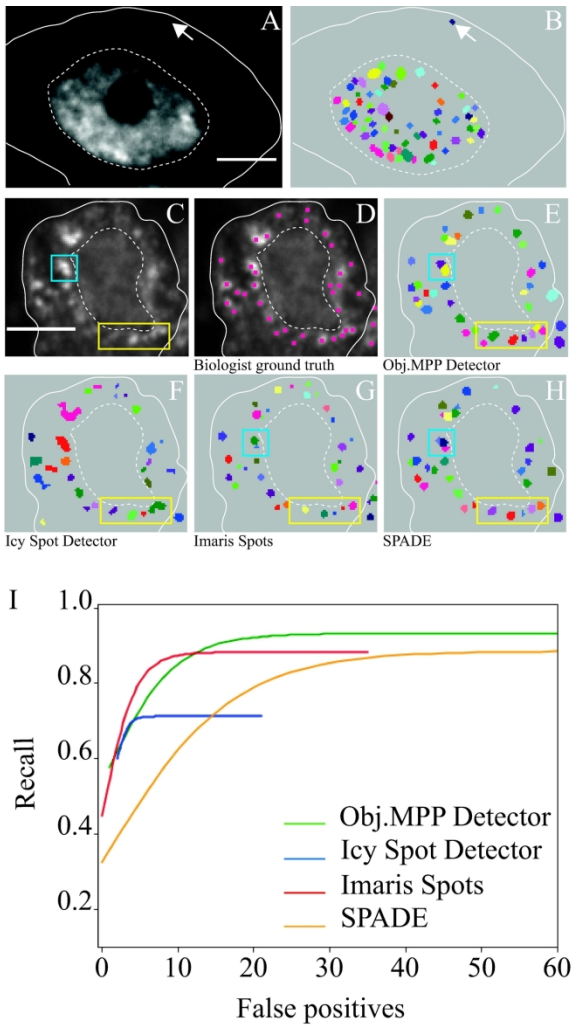


Figure 5

Figure 5. Performance of Obj.MPP in the detection of pathological stress granules on confocal images of Drosophila motor neurons

165x266mm (300 x 300 DPI)

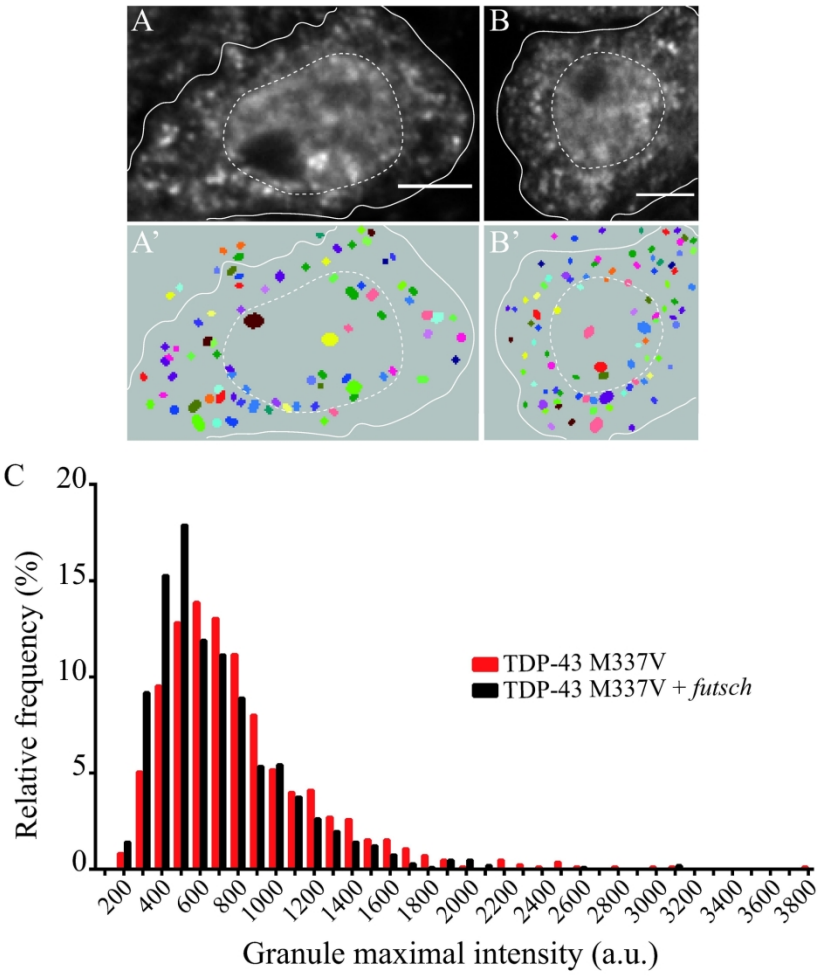


Figure 6

Figure 6. The proportion of bright TDP-43 M337V granule-like assemblies decreases upon futsch overexpression.

174x238mm (300 x 300 DPI)

## Supporting Information

### Available object shapes and associated parameters.

Shapes parameters have to be set according to the chosen object geometry as summarized in the table.

| Object type | Shape | Equations | Parameters |
|---|---|---|---|
| Disk |  | $(x-x_c)^2+(y-y_c)^2 \leq R^2$ | Radius: $R$ |
| Square |  | $\lvert X_\theta \rvert \leq S$<br>$\lvert Y_\theta \rvert \leq S$ | Side: $S$ |
| Ellipse |  | $\frac{{X_\theta}^2}{a^2}+\frac{{Y_\theta}^2}{b^2} \leq 1$ | Semi minor axis: $a$<br>Major minor ratio: $\alpha=\frac{b}{a}$<br>Angle degree: $\theta$ |
| Rectangle |  | $\lvert X_\theta \rvert \leq a$<br>$\lvert Y_\theta \rvert \leq b$ | Semi minor axis: $a$<br>Major minor ratio: $\alpha=\frac{b}{a}$ |
| Superquadric |  | $\frac{{X_\theta}^p}{a^2}+\frac{{Y_\theta}^q}{b^2} \leq 1$ | Semi minor axis: $a$<br>Major minor ratio: $\alpha=\frac{b}{a}$<br>Minor exponent: $p$<br>Major exponent: $q$<br>Angle degree: $\theta$ |
| $X_\theta=(x-x_c)\cos\theta-(y-y_c)\sin\theta,\ Y_\theta=-(x-x_c)\sin\theta-(y-y_c)\cos\theta$ | | | |

**Marked Point Process Principles:**

Consider an image :

$$I : L \rightarrow \{1,\ldots,NL\} \times \{1,\ldots,NP\}$$
$$(x,y) \mapsto I(x,y)$$

Denote by K the compact space $[1,NL] \times [1,NP]$ and by M the space of marks $M \subset \mathbb{R}^n$, n being the number of marks. An object O is an element of $L \times M$. Let $\Omega_n$ be the configurations of n objects $\Omega_n = (L \times M)^n$. The set of configurations, sets of an unknown number of objects in the image plan, is given by :

$$\Omega = \emptyset \cup \bigcup_n \Omega_n$$

We define a marked point process on $\Omega$ through a density function, with respect to the Poisson measure [1]:

$$f : \Omega \rightarrow \mathbb{R}$$
$$O \mapsto f(O)$$

The density is written in a Gibbs form $f(O) = exp\ -\ U(O)$ , where U is the energy function, also named objective function in this paper. The lowest $U(O)$ the highest probable configuration $O$ . The energy function is written as follows:

$$U(O)\ =\ \sum_i u_1(O_i)\ +\ \sum_{i \sim j} u_2(O_i,O_j)$$

The first term refers to the data term and measures how well each object fits to the data. The latter term describes interactions between neighboring objects, and for example fosters or penalizes overlaps between objects.

The different quality functions $Q(O)$ :

**1) Geometric (gradient-based)**

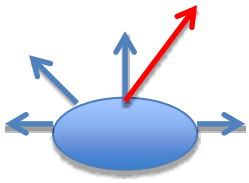

Blue arrows : normal to the object edge $\vec{n}$
Red arrows : gradient (derivative) of the intensity image $\nabla I$, variance in the object : $\sigma^2$

***1.a : Dark Object on bright Background***

*1.a.a : linear*

$$Q(O)\ =\ \frac{\int \nabla I.\vec{n}(t)dt}{\sqrt{\sigma^2\ +\ \varepsilon}}$$

*1.a.b : not linear*

Compute for all the pixels along the edge of the object the scalar product $\nabla I.\vec{n}(t)$. Consider the thirty percent bigger. Among them if a chain of neighboring pixels is bigger than a given threshold then give a high value to $Q(O)$ , else :

$$Q(O) = \frac{\int \nabla I.\vec{n}(t)dt}{\sqrt{\sigma^2 + \varepsilon}}$$

***1.b : Bright Object on dark Background***

*1.b.a : linear*

$$Q(O) = \frac{-\int \nabla I.\vec{n}(t)dt}{\sqrt{\sigma^2 + \varepsilon}}$$

*1.b.b : not linear*

Compute for all the pixels along the edge of the object the scalar product $\nabla I.\vec{n}(t)$. Consider the thirty percent lower. Among them if a chain of neighboring pixels is bigger than a given threshold then give a high value to $Q(O)$ , else :

$$Q(O) = \frac{-\int \nabla I.\vec{n}(t)dt}{\sqrt{\sigma^2 + \varepsilon}}$$

**2) Radiometric (contrast-based):**

| **Full object** | **Partial object** |
|---|---|
| 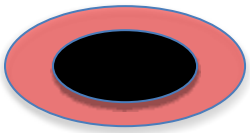 <br>Black ellipse : object (mean : $\mu_o$ variance : $\sigma_o^2$)<br>Red crown : neighborhing pixels (mean : $\mu_n$ variance : $\sigma_n^2$) | 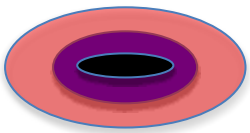 <br>Purple ellipse : interior border of the object (mean : $\mu_b$ variance : $\sigma_b^2$)<br>Red crown : neighborhing pixels (mean : $\mu_n$ variance : $\sigma_n^2$) |
| ***Dark Object on bright Background***<br>*a : un-normalized*<br>$Q(O) = \mu_o - \mu_n$<br>*b : normalized*<br>$Q(O) = \frac{\mu_o - \mu_n}{\sqrt{\sigma_o^2 + \sigma_n^2}}$ | ***Dark Object on bright Background***<br>*a : un-normalized*<br>$Q(O) = \mu_b - \mu_n$<br>*b : normalized*<br>$Q(O) = \frac{\mu_b - \mu_n}{\sqrt{\sigma_b^2 + \sigma_n^2}}$ |
| | |

| ***Bright Object on Dark Background*** | ***Bright Object on Dark Background*** |
|---|---|
| *a : un-normalized* | *a : un-normalized* |
| $$Q(O) = \mu_n - \mu_o$$ | $$Q(O) = \mu_n - \mu_b$$ |
| *b : normalized* | *b : normalized* |
| $$Q(O) = \frac{\mu_n - \mu_o}{\sqrt{\sigma_o^2 + \sigma_n^2}}$$ | $$Q(O) = \frac{\mu_n - \mu_b}{\sqrt{\sigma_b^2 + \sigma_n^2}}$$ |

**Reference**

1. Stoyan D., Kendall W., J. M. Stochastic Geometry and its Applications. *Wiley, Chichester*. 1995.

**A**

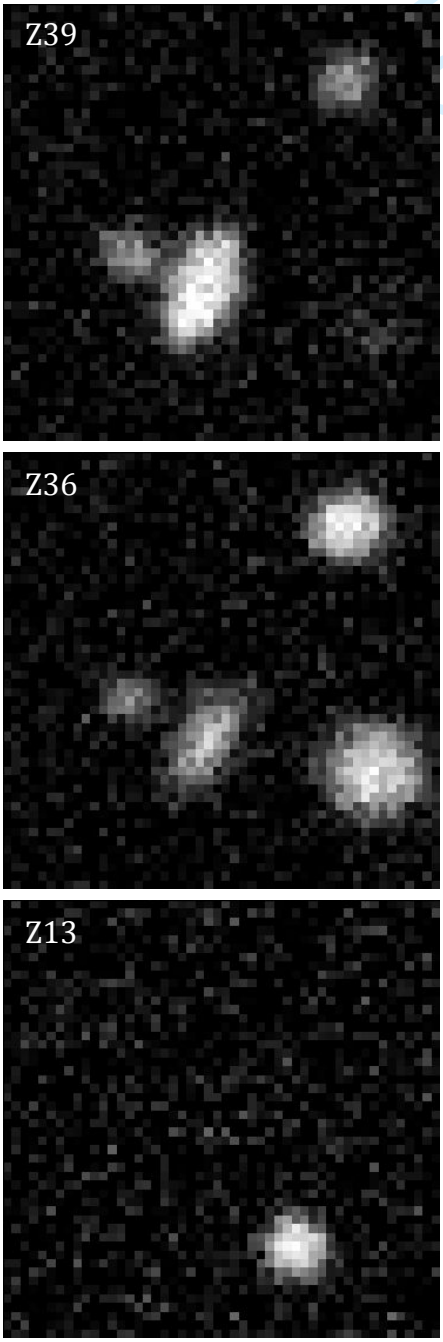


**B**

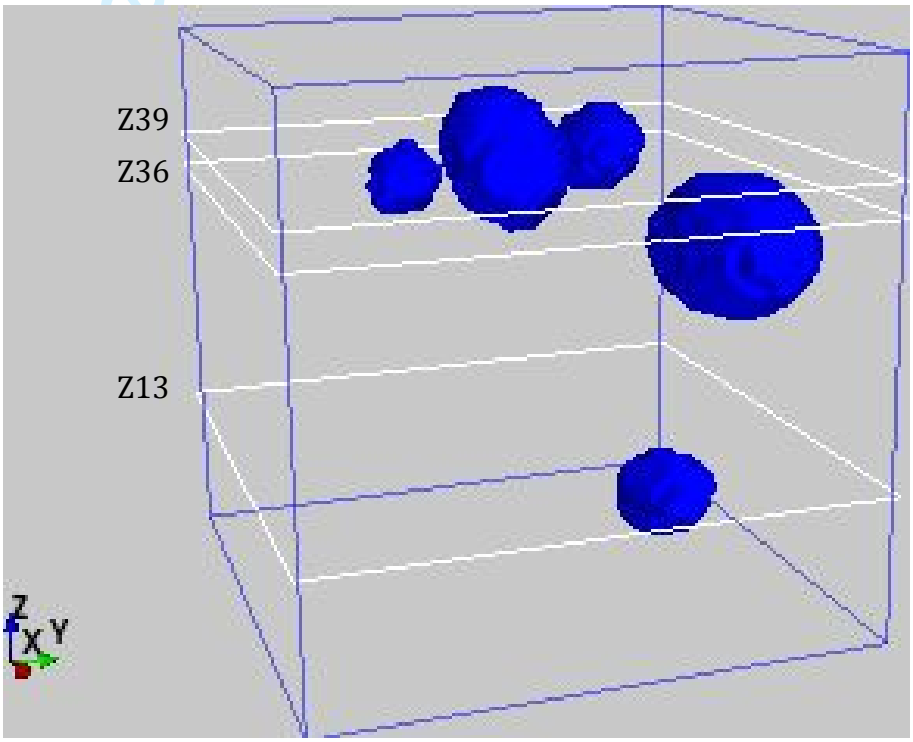

**3D object segmentation *via* the Marked Point Process.**

(A) A stack of synthetic images with objects of variable sizes was generated. Shown are three slices whose position in the stack are indicated. (B) 3D-segmentation. The position of the three slices shown in (A) is indicated. Obj.MPP parameters used in this segmentation were: 10 000 iterations, 50 births per iteration, Object type : ellipsoïd, Object ranges : semi_minor_axis_range (2, 6, 0.5), major_minor_ratio_range (1.0, 1.5, 0.025), third_minor_ratio_rng = (0.6, 1.5, 0.025), Object quality : bright on dark contrast, min_quality: 50.

**Supplemental Figure legends.**

**Figure S1. *Obj.MPP* outperforms global and local thresholding methods in the detection of heat-induced PABP-containing granules in *Drosophila* S2R+ cell line.**

(A-A') Distribution of PABP-containing granules in *Drosophila* S2R+ cells subjected to heat shock. Cells were imaged using an Olympus-Yokogawa Spinning confocal microscope and individual cells manually cropped and annotated by experimented biologists (B,B'). Shown are maximal intensity projections of original (top) or deconvolved (bottom) images. Scale bar: 3 μm. (C-I') Masks of the objects detected with *Otsu* (C,C') or *Shanbhag* (D,D') automatic global thresholding, Midgrey (E,E') or Mean (F,F') automatic local thresholding, Midgrey (G,G') or Mean (H,H') optimized local thresholding and *Obj.MPP* (I,I'). Parameters used in G:radius = 9, parameter 1 = -5 ; G':radius = 15, parameter 1 = 25, H: radius = 7, parameter 1 = -40 ; H': radius = 8, parameter 1 = -30 and I,I': 1500 iterations, 1500 births per iteration, Object type: superquadric, Object ranges: semi_minor_axis_range (2, 6, 0.25), major_minor_ratio_range (1.0, 1.0, 0.025), exponent_range (1, 2, 0.1), angle_degree_range (0.0, 179.9, 5.0), Object quality : bright on dark gradient, min_quality: 1.6. (J) Distribution of F1 scores obtained on 5 representative original (black) or deconvolved (grey) images using the same parameters as in (G-I'). Data are represented using the box and whiskers "min to max" convention, where the middle line defines the median and the whiskers go down to the smallest value and up to the largest. Individual data points are represented with symbols. Automatic global or local thresholding approaches are not optimal in the detection or individualization of granules of interest. Even after optimization of local thresholding, *Obj.MPP* still outperforms these methods in the segmentation of PABP granules. The yellow square highlights clustered granules that are individualized by *Obj.MPP*, but not by Midgrey nor Mean local thresholding (G-I' compare to A). The blue square highlights granules whose contours are under-detected or not properly defined by local threshold Midgrey and Mean (G-H' compare to A).

**Figure S2. *Obj.MPP* detects an increase in both number and size of PABP-containing granules in *Drosophila* S2R+ cells upon heat shock.**

(A, C) Distribution of PABP-containing granules in *Drosophila* S2R+ cells subjected (C) or not (A) to heat shock. Maximal intensity projections of original images are shown. Scale bar: 3

μm. The plain line delimits the cell contour. (B, D). Masks of the objects detected with *Obj.MPP*. Images were analyzed with *Obj.MPP* parameterized so as to detect a minimal number of false positives in the control images (Quality function = 2.5). (E-F) Distribution of granule numbers normalized by cell area (E) and granule sizes (F). Data are represented using scatter dot plots where the middle line defines the mean and the whiskers the standard deviation. ***, $P<0.001$ (Mann-Whithney test). Numbers of cells analyzed per condition: 34 (RT: Room Temperature), 35 (HS: Heat Shock). a.u. stands for arbitrary unit. Numbers of granules analyzed per condition: 471 (RT) and 1511 (HS)

**Figure S3. FROC curves (raw data)**

Average FROC curves (see section 4-1) generated for the different tested algorithms by varying the detection threshold values on five representative original (A) or deconvolved (B) images of *C. elegans* and five representative original images of *D. melanogaster* (C). Best F1 scores obtained for each image and their corresponding threshold (quality) values are shown in Table S1.

**Figure S4. Characteristics of heat-induced CAR-1 granules in *C. elegans* and of TDP-43 M337V granule-like assemblies in *Drosophila menalogaster*.**

(A) Percentages of CAR-1 granules bigger than 35 pixels (defined arbitrarily) in the presence (left) or absence (right) of PUF-5. Error bars represent s.e.m. ***, $P<0.001$ (Fisher's exact test). Numbers of granules analyzed: 680 and 533 for the +HS and +HS *puf-5* RNAi conditions respectively. (B,C) Distributions of the number (B) and size (C) of Venus- TDP43-M337V aggregates in the absence (left) or presence (right) of *futsch* overexpression. Numbers were normalized to surface area. a.u. stands for arbitrary unit. Sizes were measured in pixels. Box plots are represented using the "min to max" convention, where the middle line defines the median and the whiskers go down to the smallest value and up to the largest. Individual values are plotted on top of the box plots in C. n.s. stands for not significant (t-test). Numbers of cell bodies analyzed in B: 61 for the TDP-43 M337V and 60 for the TDP-43 M377V + *futsch* overexpression conditions respectively. Numbers of granules analyzed in C: 851 for TDP-43 M337V sole expression and 1068 for TDP-43 M377V and *futsch* overexpression. Parameters used for detection with *Obj.MPP* are described in the legend of Figure 5. (D) Percentages of TDP-43 M337V-containing granules showing a maximal fluorescence intensity above 900 (defined arbitrarily) in motor neuron cell bodies in the presence (right) or absence (left) of *futsch* overexpression. Error bars represent s.e.m. ***,

*P*<0.001 (Fisher's exact test). Numbers of granules analyzed: 851 for TDP-43 M337V sole expression and 1068 for TDP-43 M377V and *futsch* overexpression.

**Table S1. Best F1 scores obtained by the algorithms for the different biological images tested**

Indicated are, for each algorithm and each set of data (*C. elegans* oocytes and *Drosophila melanogaster* motorneurons), the thresholds identified to obtain the best F1 score for each biological image analyzed and the mean and standard deviation of the best F1 scores.

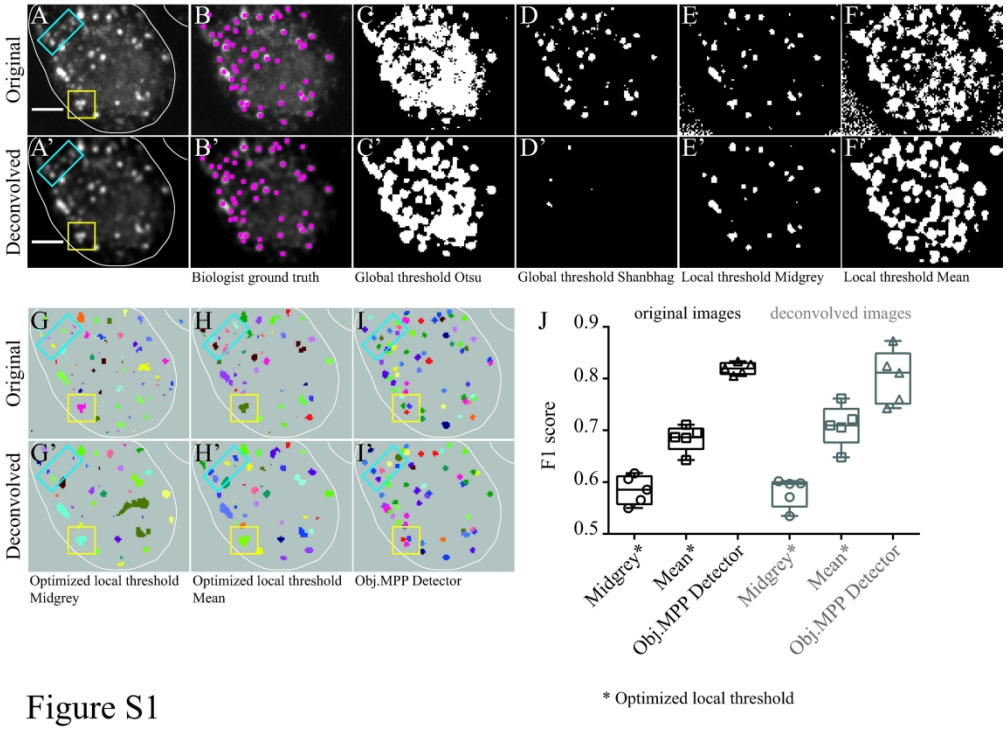


Figure S1

245x178mm (300 x 300 DPI)

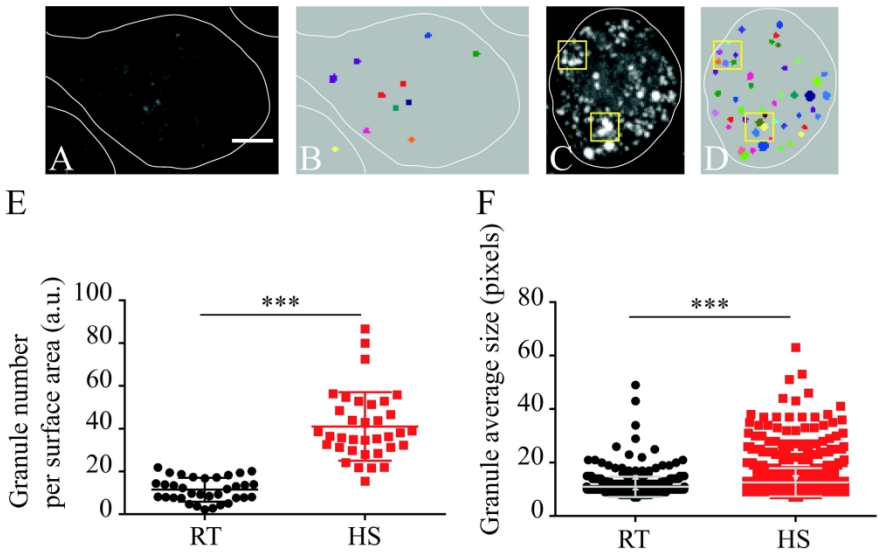


Figure S2

237x160mm (300 x 300 DPI)

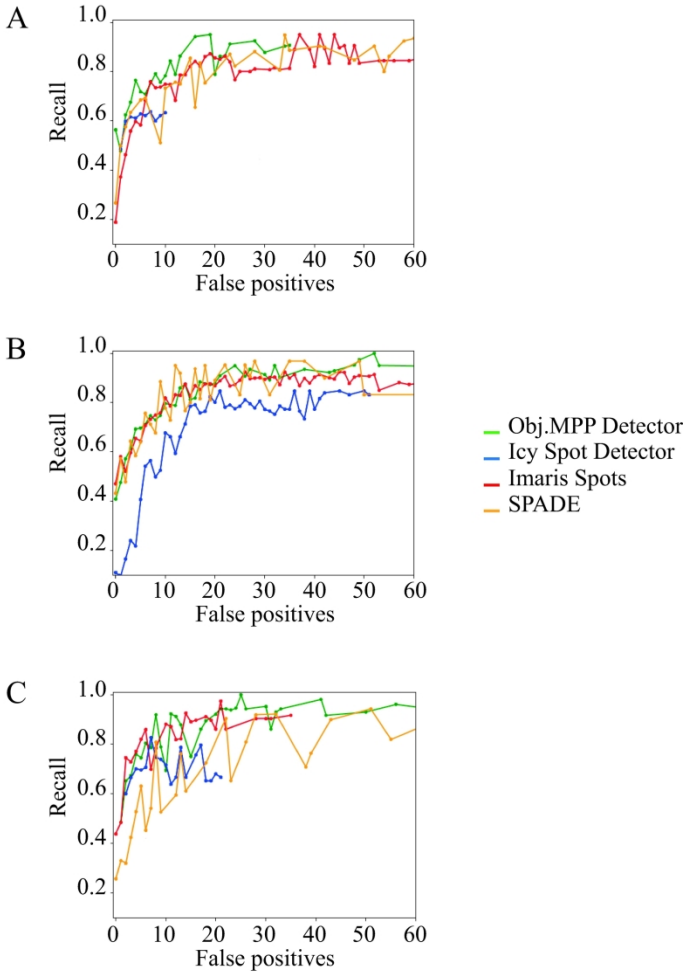


Figure S3

184x322mm (300 x 300 DPI)

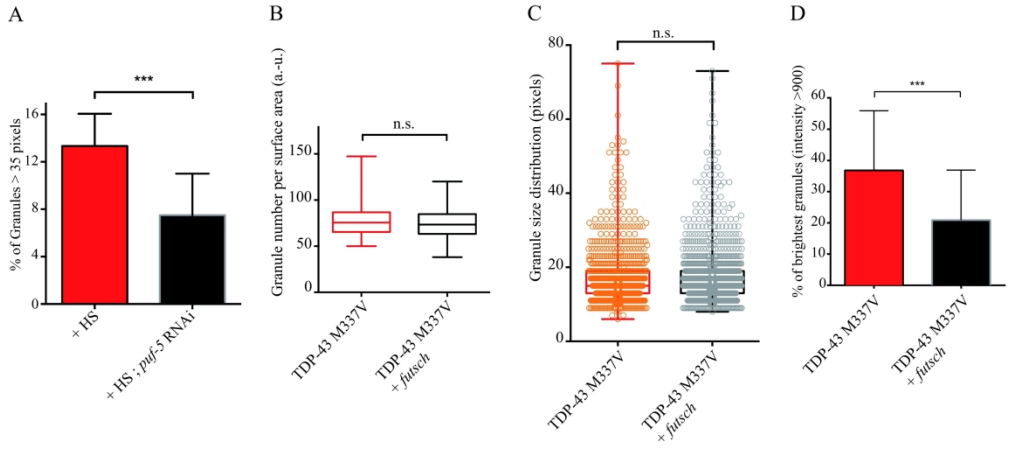


Figure S4

291x176mm (300 x 300 DPI)

| | *C. elegans* | Icy | | Imaris | | Obj.MPP | | Spade | |
|---|---|---|---|---|---|---|---|---|---|
| | | best F1-score | Threshold | best F1-score | Threshold | best F1-score | Threshold | best F1-score | Threshold |
| Original images | image 1 | 0,74 | 205 | 0,77 | 56 | 0,82 | 0,85 | 0,72 | 0,02 |
| | image 2 | 0,83 | 175 | 0,78 | 112 | 0,81 | 0,95 | 0,77 | 0,035 |
| | image 3 | 0,73 | 144 | 0,81 | 117 | 0,8 | 0,85 | 0,76 | 0,025 |
| | image 4 | 0,78 | 180 | 0,84 | 97 | 0,85 | 0,95 | 0,8 | 0,0225 |
| | image 5 | 0,74 | 160 | 0,85 | 134 | 0,86 | 1 | 0,82 | 0,04 |
| | Mean | 0,76 | | 0,81 | | 0,83 | | 0,77 | |
| | Std Dev | 0,04 | | 0,04 | | 0,03 | | 0,04 | |

| | *C. elegans* | Icy | | Imaris | | Obj.MPP | | Spade | |
|---|---|---|---|---|---|---|---|---|---|
| | | best F1-score | Threshold | best F1-score | Threshold | best F1-score | Threshold | best F1-score | Threshold |
| Deconvolved images | image 1 | 0,76 | 240 | 0,8 | 2100 | 0,84 | 0,9 | 0,81 | 0,14 |
| | image 2 | 0,78 | 180 | 0,83 | 2200 | 0,83 | 1,15 | 0,79 | 0,17 |
| | image 3 | 0,73 | 200 | 0,81 | 2800 | 0,79 | 1,4 | 0,85 | 0,16 |
| | image 4 | 0,74 | 160 | 0,86 | 2450 | 0,86 | 1,25 | 0,81 | 0,15 |
| | image 5 | 0,79 | 230 | 0,87 | 2850 | 0,86 | 1,05 | 0,89 | 0,2 |
| | Mean | 0,76 | | 0,83 | | 0,84 | | 0,83 | |
| | Std Dev | 0,03 | | 0,03 | | 0,03 | | 0,04 | |

| | *D. melanogaster* | Icy | | Imaris | | Obj.MPP | | Spade | |
|---|---|---|---|---|---|---|---|---|---|
| | | best F1-score | Threshold | best F1-score | Threshold | best F1-score | Threshold | best F1-score | Threshold |
| Original images | image 1 | 0,78 | 152 | 0,86 | 56 | 0,79 | 1,5 | 0,66 | 0,175 |
| | image 2 | 0,76 | 155 | 0,91 | 70 | 0,89 | 1,35 | 0,83 | 0,2 |
| | image 3 | 0,82 | 145 | 0,85 | 59 | 0,86 | 1,45 | 0,70 | 0,15 |
| | image 4 | 0,85 | 95 | 0,93 | 50 | 0,88 | 1,8 | 0,82 | 0,2 |
| | image 5 | 0,73 | 133 | 0,81 | 94 | 0,82 | 1,3 | 0,68 | 0,2 |
| | Mean | 0,79 | | 0,87 | | 0,85 | | 0,74 | |
| | Std Dev | 0,05 | | 0,05 | | 0,04 | | 0,08 | |

Table S1